ACS Catalysis

Research Article

pubs.acs.org/acscatalysis

Methanol Decomposition over Palladium Particles Supported on Silica: Role of Particle Size and Co-Feeding Carbon Dioxide on the Catalytic Properties

Selma Hokenek and John N. Kuhn*

Department of Chemical and Biomedical Engineering, University of South Florida, 4202 East Fowler Avenue, ENB118, Tampa, Florida 33620, United States

Supporting Information

ABSTRACT: Monodisperse palladium particles of six distinct and controlled sizes between 4−16 nm were synthesized in a one-pot polyol process by varying the molar ratios of the two palladium precursors used, which contained palladium in different oxidation states. This difference permitted size control by regulation of the nucleation rate because low oxidation state metals ions nucleate quickly relative to high oxidation state ions. After immobilization of the Pd particles on silica by mild sonication, the catalysts were characterized by X-ray absorption spectroscopy and applied toward catalytic methanol decomposition. This reaction was determined as structure sensitive with the intrinsic activity (turnover frequency) increasing with increasing particle size. Moreover, observed catalytic deactivation was linked to product (carbon monoxide) poisoning. Co-feeding carbon dioxide caused the activity and the amount of deactivation to decrease substantially. A reaction mechanism based on the formation of the π-bond between carbon and oxygen as the rate-limiting step is in agreement with antipathetic structure sensitivity and product poisoning by carbon monoxide.

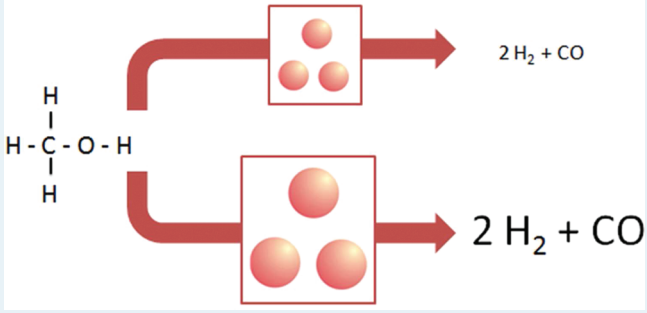

KEYWORDS: *nanoparticle growth, nucleation, structure sensitivity, methanol catalysis, product poisoning*

The primary goals in heterogeneous catalysis are the achievement of a catalyst with high selectivity for the desired product, a high activity, and a minimal deactivation rate. Due to the catalytic properties dependence upon surface structure that vary with particle size[1−3] and shape[4,5] distributions, nanotechnology-inspired strategies for the synthesis of well-defined monodisperse particles now open new avenues for the design of catalysts with desirable properties. Several studies have highlighted key demonstrations of improvements in activity[6−8] and selectivity.[5,9−12] However, the impact of nanotechnology on improving stability has proceeded with less emphasis. Porous metal oxide shells have been used to encapsulate active metal nanoparticles to improve thermal stability.[13−15] Size-dissolution[16] and composition-dissolution[17] relations have been proposed for Pt-catalyzed electrocatalytic reactions needed for fuel cell chemistry in acidic solutions. Catalyst durability under reaction conditions is perhaps the most important area and proper focus on it is needed.

In current society, an important area for these advances is in the field of energy and catalysis will be a major part in it.[18] Hydrogen generation and storage is a key topic and the use of methanol as a liquid storage and delivery agent is an option. Hydrogen is a key species for a number of current energy applications including hydrotreating and ammonia synthesis. Moreover, hydrogen is a potential cornerstone in renewable energy with disruption by fuel cells[19] and production of synthetic fuels through the thermochemical route[20] hinged on the ability to economically produce and safely store and delivery hydrogen. The use of alcohols for these needs is an option and the present work focuses on the impact of palladium particle size on methanol decomposition catalysis. Methanol, the simplest alcohol, was selected due to its ability to decompose without the need of an oxidant (e.g., air, steam, carbon dioxide) and, consequently, the impact of these factors can also be studied.

In addition to scientific merits toward understanding the aforementioned catalytic dependence on surface structure (coined structure sensitivity), the knowledge has practical implications. For example, if the intrinsic rate (catalytic cycles per active site per time or turnover frequency; TOF) increases with decreasing particle size (sympathetic structure sensitivity[21]) or is independent of particle size, the maximum rate per mass of catalyst will occur for the smallest particles. However, if the intrinsic rate were to increase with increasing particle size (antipathetic structure sensitivity[21]), a maximum rate per mass of catalyst would exist at an intermediate particle size. The

Received: December 27, 2011
Revised: March 6, 2012
Published: April 18, 2012

   dx.doi.org/10.1021/cs200689k | ACS Catal. 2012, 2, 1013−1019

latter scenario is precisely what happens in the case of Fischer–Tropsch synthesis and an optimal Co particle size near 7 nm resulted.[22,23] For the reasons outlined here, advanced synthetic procedures are needed to finely tune the particle size and the resulting properties.

A variety of approaches have been investigated in the pursuit of a method that will allow for the reproducible synthesis of precious metal and, in particular emphasis here, palladium nanoparticles with uniform size. A robust and simple approach is a one-pot polyol process which involves using an alcohol with multiple hydroxyl groups as both the solvent and reducing agent for the formation of metal nanoparticles from ionic precursors. The particle size is controlled through regulation of nucleation and growth rates, which depend on a number of factors including concentration,[24] stabilization agents,[25−27] as well as common parameters[28] like temperature and time.

In the present study, Pd particle size control is achieved in a polyol synthesis through the scientific basis of metal ions' nucleation rate increasing as the precursor oxidation state is decreasing. After synthesis of Pd particles of controlled size, the particles were immobilized onto commercial silica by mild sonication to reach 2 wt % Pd/silica catalysts, which were used for further characterization and catalytic methanol decomposition studies. The aims of this study are to demonstrate synthesis of monodisperse Pd particles by a simple and scientific approach and determine the structure sensitivity of catalytic methanol decomposition including its role in catalytic stability. The results show the steady-state activity is reached more quickly when cofeeding carbon dioxide and the TOF increased with increasing particle size. This relation yields an optimal particle near 6 nm to maximize the rate per mass of catalyst. Through the balance of surface sites per mass of metal and the antipathetic structure sensitivity, this optimal particle size is proposed for catalytic reactions involving double bonds forming or breaking as a slow kinetic step.

Scheme 1. Strategy for Control of the Pd Particle Size

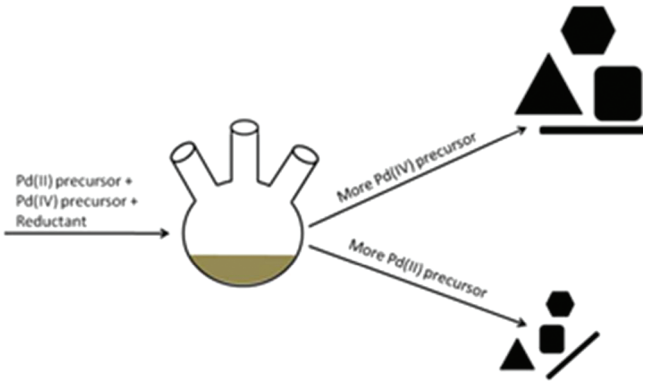

RESULTS AND DISCUSSION

Unsupported Pd Particles. Representative TEM images of the six syntheses of particle synthesized are shown in Figure 1. Although a variety of particles shapes such as shapes, including rods, triangles, and cubes existed, the dominant particle shape was polyhedral. Based on the TEM images, a metallic or zero-valence state of Pd is established. This fact is confirmed by the X-ray diffraction (XRD). The XRD profiles (Supporting Information Figure SI1) for all syntheses are consistent with zero-valence state of Pd in a face-centered cubic (FCC)

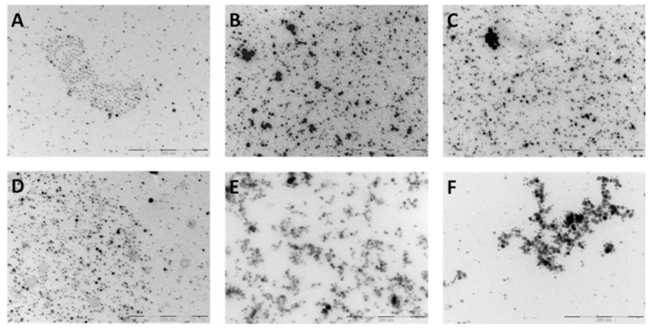

Figure 1. Representative TEM images of the unsupported Pd particles of different sizes. Scale bars represent 200 nm with subsections of 40 nm. (A) 0% Pd(IV), (B) 20% Pd(IV), (C) 40% Pd(IV), (D) 60% Pd(IV), (E) 80% Pd(IV), (F) 100% Pd(IV). In each case, the balance of Pd is Pd(II). With increasing Pd(IV) content, the particle size increased due to an increase in the growth rate relative to the nucleation rate, which is a function of the precursor oxidation state.

structure (e.g., JCPDS 46-1043). For all syntheses, the (111), (200), (220), and (311) diffraction lines at two values of 40°, 47°, 68°, and 82°, respectively, indicate a lattice parameter (a) near 3.89 Å. This lattice parameter yielded a Pd–Pd bond distance of 2.75 Å, which is the expected value[29] of a bulk Pd material with a FCC structure.

The TEM images and XRD profiles are also used to quantify the particles sizes from all syntheses. Qualitatively, as observed in Figure 1, the Pd particle size increased as the ratio of Pd (IV): Pd (II) increased. A statistical analysis for each synthesis is reported in Figure 2 and the increase in particle size

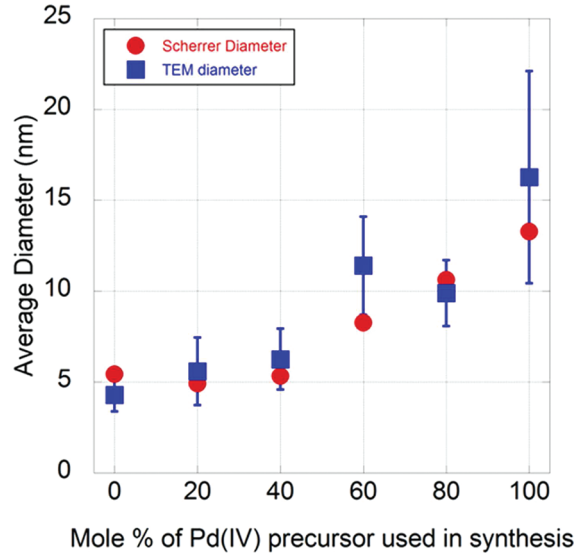

Figure 2. Average particle diameter calculated from TEM images (Figure 1) with one standard deviation and XRD line broadening (Supporting Information Figure S1). In each case, the balance of Pd is Pd(II).

proportional to the ratio of Pd (IV): Pd (II) is evident. As expected, the standard deviation increased slightly with increasing particle size. However, each standard deviation was 35% or less relative to the mean particle size value for all of the syntheses and these values represent good achievement of monodisperse particles. The particle sizes calculated from XRD line broadening (the Scherrer equation; Figure 2) yielded the

dx.doi.org/10.1021/cs200689k | ACS Catal. 2012, 2, 1013–1019

same trend, with particle size being a strong function of the Pd (IV): Pd (II) ratio, as compared to the TEM analysis. The mean particle sizes obtained from TEM were used to calculate the dispersion (Table 1) using a standard[30] surface area-size relationship.

Table 1. Precursor Ratios, Sizes, and Dispersions for Syntheses of Size-Controlled Pd Nanoparticles

sample					
Pd(IV) (%)	Pd(II) (%)	size (nm)[a]	dispersion (%)[b]	coordination number[c]	interatomic distance (Å)[c]
0	100	4.3 ± 0.9	25.7	10.1	2.740
20	80	5.6 ± 1.9	19.7	10.2	2.741
40	60	6.3 ± 1.7	17.5	10.3	2.740
60	40	11.4 ± 2.7	9.6	11.0	2.742
80	20	9.9 ± 1.8	11.1	10.5	2.742
100	0	16.3 ± 5.8	6.8	11.6	2.749

[a]Determined from TEM analysis (unsupported Pd NPs). [b]Calculated using average TEM particle size. [c]Determined from EXAFS analysis (supported Pd NPs).

The key advantage of this synthesis approach is that well-defined particles were obtained in a scientific manner with a simple synthesis using one adjustable variable. That is, Pd particle size control has been demonstrated by just altering the oxidation state of the Pd precursor. All other conditions were identical for all of the colloidal syntheses in this work. A similar approach[5] was performed for Pt particles synthesized with simultaneous size and shape control. Thus, the versatility of this strategy may provide a platform for the synthesis of other metals as well. A key difference between the study on Pt[5] and the present study is the trend that occurs as a function of the precursor's oxidation state. For Pt, the change in particle size with the precursor ratio was linear. For the Pd particles synthesized in this work, the trend appears either nonlinear (order greater than 1) or linear above a threshold value of about 40% Pd (IV). Since many factors that influence the nucleation rate also alter the growth rate,[31,32] the exact fundamental underlying source for the differences in the two studies is difficult to pinpoint.

Silica-Supported Pd Particles. XAS was conducted to characterize the Pd particles after immobilization on silica at 2 wt %. Both the XANES (Supporting Information Figure SI2) and the EXAFS (Supporting Information Figure SI3) regions indicate the zero-valence metallic state regardless of Pd particle size was maintained. This conclusion was reached for the following reasons. The XANES region intensity (peak at 24365 eV in Figure SI2) is lower than the first contribution to the EXAFS region (peak at 24390 eV in Supporting Information Figure SI2). The XANES region intensity generally increases compared to the EXAFS region intensity as the oxidation state of the target atom increases and this trend is due to bonding atoms being closer to the central atom for oxidized atoms. Thus, the likelihood of multiscattering events increases.[33] Moreover, the EXAFS resonance matches well, both qualitatively and quantitatively, to that of a Pd foil.

Using the Pd foil as a reference material, a complete EXAFS analysis was performed (see Supporting Information and Table SI1 for complete details) and the two key output parameters, the Pd coordination number and the Pd interatomic distance, are summarized in Table 1. For metallic Pd in a FCC structure, the interatomic distance is equivalent to the Pd−Pd bond length. The interatomic distances calculated from the Pd K edge correspond well to the value calculated from XRD. The Pd−Pd coordination numbers for the Pd particles fall in the expected range of between 9 (Pd−Pd coordination of (111) surface) and 12 (Pd−Pd coordination in bulk FCC Pd). A slight trend existed with Pd−Pd coordination numbers increasing with particle size increasing. The fact that the Pd−Pd coordination numbers fall in the expected range for particles of these sizes indicate limited, if any, change in the particle structure after immobilization. Minimal support interactions are expected for precious metals on silica. Moreover, the results suggest minimal restructuring, such as the formation of islands, on the silica support. In essence, the XAS indicate particles properties consistent with the characterization of the unsupported Pd particles, so the results of the unsupported Pd particles are applied to the metal supported catalysts.

Catalytic Methanol Decomposition. Methanol decomposition rates are presented in two different formats in Figure 3.

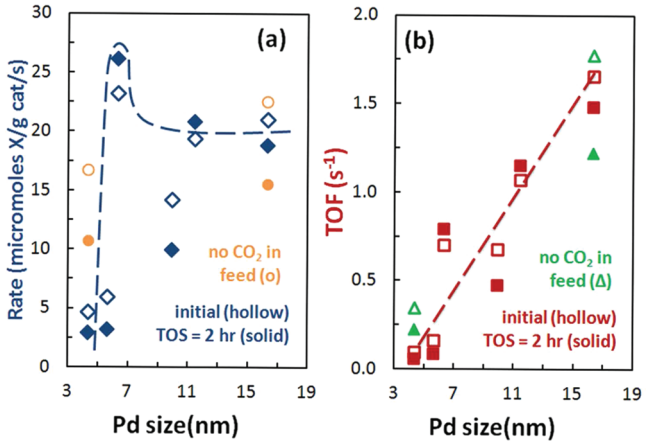

Figure 3. Methanol (a) conversion rates and (b) turnover frequencies (TOF) of 2 wt % Pd/silica as a function of Pd particle size, carbon dioxide in the feed, and time-on-stream (TOS) at T = 350 °C.

In Figure 3a, the methanol conversion obtained under differential conditions was normalized per the total mass of catalyst to yield a reaction rate. In Figure 3b, the methanol conversion obtained under differential conditions was normalized per the surface atoms of palladium to yield the intrinsic activity or turnover frequency (TOF). Moreover, the activities are reported by the initial conversion (hollow points) and conversion after 2 h on stream (solid points). Finally, the activities are compared with and without carbon dioxide added with the carbon dioxide-free experiments represented by circles in Figure 3a and triangles in Figure 3b. Lower activity and less deactivation were measured for when carbon dioxide is cofed. From these results, Pd particle size, the addition of carbon dioxide, and time-on-stream all demonstrated an influence on the activities.

The TOF trend in Figure 3b follows the activity-size trend classically[21] called negative particle size effects or antipathetic sensitivity. The trend simplistically means that the approximate surface residence time of the surface species in the rate-determining step is longer on the surfaces of the small particles as compared to the surfaces of the large particles. Because of the opposite trend of increasing metal surface per increasing particle size, antipathetic sensitivity trends naturally yield a

dx.doi.org/10.1021/cs200689k | ACS Catal. 2012, 2, 1013−1019

maximum rate per mass of catalyst at in intermediate particle size (~6 nm as observed in Figure 3a). A greater discussion on this topic and its relevance to the catalytic mechanism is given in the next section.

Since the catalysts (only the catalysts with the smallest and largest Pd sizes) demonstrated deactivation with time-on-stream, carbon dioxide was cofed with methanol to test its effect on the stability. The addition of carbon dioxide decreased both the activity and the deactivation amount. With coking a possible reason for the catalyst deactivation and the difference in activity with and without carbon dioxide cofed, postreaction TPO experiments (T_{max} =500 °C) were performed and coking rates were calculated from the intensities of carbon dioxide signals. The coking rates calculated from the TPO experiments are compared to the methanol conversion rates in Supporting Information Figure SI4. For all catalysts, the methanol reaction rate is greater than the coking rate and the difference is by more than an order of magnitude for the more active catalysts. Also, the amount of coke generated from the spent sample was on the same order of magnitude as the carbon produced during the pretreatment oxidation step. This comparison further supports coking is not a strong factor in the deactivation process. The coking rate per catalyst mass does not show a Pd particle size trend and, thus, the rate per Pd surface area would be diluted for the catalysts where the two rates are on the same order of magnitude. The lack of coking is also supported by positive (unfavored) dissociative chemisorption energies of CO and CO_2 on a Pd (211) single crystal surfaces.[34]

In addition to TPO, several other experiments were performed after the catalysts were used for methanol decomposition. When methanol decomposition was repeated on the post-TPO catalysts (TPO experiments with T_{max} =500 °C), the methanol decomposition rates decreased compared to the first catalytic reaction. This activity decrease was associated to aggregation of Pd particles. This conclusion was reached because oxidation at temperatures of 500 °C should be able to remove almost all types of carbon species[35] and because the activity loss was more pronounced for the small particles that should be more susceptible to aggregation. However, when a postreaction TPO was performed at a low temperature (T_{max} = 350 °C), the activities and deactivation profiles were reproducible to the first catalytic trial regardless of Pd size even though the temperature was not high enough to remove all coke-related carbon. In the absence of a postreaction oxidation treatment, a repeat of the reaction cycle led to the same steady-state activity and no deactivation (the activity went straight to the steady level as the temperature reached 350 °C). These results also demonstrate that the development of strong support interactions, which are not expected for Pd on silica, did not occur at temperature below 350 °C. Therefore, carbon monoxide poisoning seems to be the only reasonable route for the catalyst deactivation. Carbon monoxide is known[36] to bond very strongly to transition metal surfaces. In light of the structure sensitivity trends, additional support for this explanation is discussed in the next section.

Structure Sensitivity and Insight into the Catalytic Mechanism. The deactivation mechanism is caused by carbon monoxide poisoning. With hydrogen present, carbon dioxide likely contributes to the activity loss by generating a small amount of carbon monoxide through the reverse-water gas shift reaction. The addition of carbon dioxide to the feed or as a pretreatment step may serve as a manner to limit deactivation in hydrocarbon conversion catalysis. Carbon dioxide's role would be equivalent to dosing poisons as is done in several other applications including purposeful sulfur poisoning[37,38] to limit coke formation during methane-steam reforming.

As demonstrated above, regardless of cofeeding carbon dioxide, methanol decomposition demonstrated antipathetic structure sensitivity. For monometallic catalysts without strong support interactions, surface structureor roughness and ensemble behaviors are typical culprits for structure sensitivity.[21] Since the Pd particles in the current study are greater than 4 nm in size and the effect of surface structure is minimal for particles of ~4 nm or greater (e.g., octahedron[21] and cuboctahedron[39]), ensemble behaviors are more likely to contribute to the structure sensitivity than surface structure arguments.

On the basis of analysis of trends in the literature, structure sensitivity occurred through particle size induced adsorbate surface coverage changes, which are fundamentally initiated from an ensemble effect. The antipathetic behavior is associated to the formation of a π-bond[2] between carbon and oxygen that is produced as the carbon−oxygen surface intermediate is dehydrogenated. The d-band center is a function of metal particle size with the d-band center moving toward the Fermi level as the particle size decreased. This trend is chemically validated as strong adsorbate−surface bonds form as the d-band center moved closer to the Fermi energy because the valence electrons become more localized on the surface metal atoms and the metal is more willing to share electrons with the adsorbate molecules.

To quantify these trends in coordination to the current efforts, a reaction energy diagram was constructed using a semiempirical approach[40] to approximate the d-band center of the surface Pd atoms and available literature on the binding energies of methoxy[36] and molecular carbon monoxide[41] species as a function of the d-band center for transition metal surfaces. In addition to parameters particular to Pd,[42] the only other input into the existing model[40] was the Pd−Pd coordination in the surface layer, which was obtained by varying particle size assuming a cuboctrahedral geometry. The bulk and surface coordination numbers calculated from experimental results and from geometric models are compared on Supporting Information Table SI2. The d-band center of the surface Pd atoms ranged from −2.1 eV (4.3 nm Pd) to −2.26 eV (16.3 nm Pd), which is general agreement with Pd surfaces.[36,43] Using linear relationships in the literature[36,41]for relating binding energies as a function to the d-band center, the adsorption energies of molecular carbon monoxide and dissociatively adsorbed methanol were established. The calculations are compiled into the reaction energy diagrams in Figure 4 (only the largest and smallest Pd particles shown; see Supporting Information Table SI3 for complete comparisons). The energy changes associated to the dehydrogenation steps are neglected. This assumption was made because the antipathetic structure sensitivity implies the activation of a molecular π-bond in the rate determining step[2] and reactions between an adsorbed hydrogen atom with a surface intermediate does not strongly influence energy changes for other reactions.[34] Consequently, the reaction energetics (ΔE) is largely driven by the change in the interactions between carbon−oxygen moieties adsorbed on the surface. Using the Brønsted−Evans−Polanyi linear activation energy-free-energy relationship,[34,44] the lower barrier for the rate-determining step on the surfaces of the larger particles relative to the surfaces of

dx.doi.org/10.1021/cs200689k | ACS Catal. 2012, 2, 1013−1019

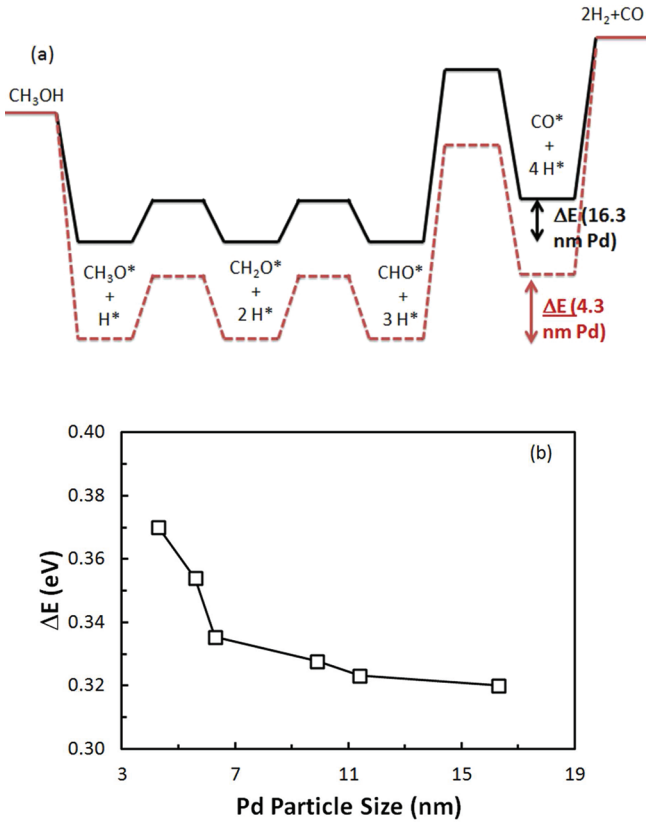

Figure 4. Reaction energy differences for methanol decomposition as a function of Pd size. (a) Reaction energy diagrams for the largest and smallest sizes. A lower energy change for the surfaces for the large Pd particles (solid, black lines) relative to the surfaces of the small Pd particles (dashed, red line) indicate a higher intrinsic activity for the large Pd particles. (b) The decreasing energy barrier trend exists with increasing Pd particle size.

the smaller particles corresponds to a proportionally lower activation energy.

CONCLUSION

The current work demonstrates the application of nanotechnology in designing catalysts with improved activity and stability. Well-defined palladium particles of controlled size between 4 - 16 nm were synthesized by a simple one-pot polyol synthesis. The difference in nucleation rates as a function of the palladium precursor's oxidation states were used to scientifically control the particle size. The palladium particles were immobilized onto silica and used in the gas-phase catalytic decomposition of methanol, which was determined to be structure sensitive and susceptible to deactivation. The intrinsic activity (turnover frequency) increased with increasing particle size. Since cofeeding carbon dioxide caused the activity and the amount of deactivation to decrease substantially and coking was assessed not to be prevalent, the observed catalytic deactivation was linked to product (carbon monoxide) poisoning. In light of the antipathetic structure sensitivity and product poisoning by carbon monoxide, a reaction mechanism based on the formation of the π-bond between carbon and oxygen as the rate-limiting step was proposed. This mechanism was modeled using a simple semiempirical relation between coordination number and d-band center of palladium and it predicts increasing activity with increasing palladium particle size.

METHODS SECTION

Chemicals. Ammonium hexachloropalladate (IV) ($(NH_4)_2PdCl_6$, 99%; Sigma-Aldrich), ammonium tetrachloropalladate (II) ($(NH_4)_2PdCl_4$, 99%; Sigma-Aldrich), poly(vinylpyrrolidone) (PVP, M_w = 40 000; Sigma-Aldrich), tetramethylammonium bromide (TMAB; $N^+(CH_3)_4Br^-$, >98%; Sigma-Aldrich), ethylene glycol (>98%; Sigma-Aldrich), and analytical grade solvents including acetone, ethanol, methanol, and hexanes were used as received without further purification. All gases (Airgas) were ultrahigh purity grade.

Synthesis. The polyol synthesis was performed using ethylene glycol as the solvent and reducing agent. After addition of the desired mass of the palladium precursors, PVP, and TMAB to 10 mL of ethylene glycol contained in a round-bottom flask, the solution was purged of dissolved oxygen by aggressively bubbling Ar for 30 min. The molar ratio of reactants, Pd: TMAB: PVP, was 1:10:40 with the total Pd (palladium precursors were altered as described in Table 1) amount being 50 μmol and the PVP amount being in terms of the repeating unit. Then, the solution was lowered an oil bath maintained at 180 °C by heating on a hot plate and held at this temperature for 20 min. The solution was cooled by removing the flask from the oil bath. The particles were then precipitated with an excess (90 mL) of acetone. The supernatant was then removed, and the particles were resuspended in ethanol and washed three times, alternating between hexane and ethanol to remove the excess stabilizing agents. After washing, the particles are resuspended in 20 mL of ethanol.

These particles were immobilized on high surface area silica (Cab-O-Sil, ~250 m^2/g). The Pd loading in all cases was 2 wt % Pd with a balance of silica. To deposit the particles, the ethanol-dispersed particles were added to the mass of silica calculated based on the mass of Pd per volume of suspension. The slurry was sonicated at room temperature for 60 min to ensure an even mixing of the suspended nanoparticles and the silica support. The resulting material was centrifuged at 6500 rpm for 15 min and the supernatant discarded. The resulting gel was dried and crushed into a fine powder for use in catalytic experiments.

Characterization. The Pd morphology was studied using X-ray diffraction (XRD), transmission electron microscopy (TEM), and X-ray absorption spectroscopy (XAS). XRD was performed using a Philips PANalytical X-Pert Pro X-ray diffractometer with a Cu Kα X-ray source. Samples were analyzed using a step size of 0.1 degrees and a dwell time of 10 s. TEM images were taken at acceleration voltages of 60 kV, and magnifications ranging from 71k× to 180k× using an FEI Morgagni 268D microscope. A particle size distribution was measured for each synthesis by measuring the particle size of 100 particles. The diameter of each particle was measured twice, with both measurements at right angles to one another, and the measured values were averaged to get the nominal particle diameter included in the histograms made for each sample. The resulting histogram was fitted with a Gaussian distribution function to arrive at the average particle size and standard deviation (SD).

XAS was performed at DuPont-Northwestern-Dow (DND) Collaborative Access Team (CAT) beamline 5-BM-D (BM = bending magnet, http://www.dnd.aps.anl.gov/) at the Advanced Photon Source, Argonne National Laboratory using the procedures, including the Athena software package,[45,46] as described in the Supporting Information. TEM and XRD were

dx.doi.org/10.1021/cs200689k | ACS Catal. 2012, 2, 1013–1019

performed on unsupported particles whereas XAS was conducted on the silica-supported particles.

Catalytic Studies. Catalytic methanol decomposition was performed with a laboratory-scale, fixed-bed quartz U-tube flow reactor enclosed within a Thermolyne furnace. A type-K thermocouple was used to measure the temperature on the bottom of the quartz wool plug that supported the catalyst. Gas flows were controlled by calibrated mass flow controllers (Alicat Scientific). Prior to the catalytic measurements, the catalysts were treated in a flow of 5 SCCM of oxygen and 45 SCCM of helium during a temperature program from room temperature to 350 °C with a ramp rate of 10 °C/min and a 1 h hold. For experiments without carbon dioxide, a total flow of 76 SCCM was used and it was comprised of 3.8 SCCM of methanol and 72.2 SCCM of helium. For experiments with carbon dioxide, a total flow of 76 SCCM was used and it was comprised of 3.8 SCCM of methanol, 3.8 SCCM of carbon dioxide, and 68.4 SCCM of helium. The combined gases were introduced into the reactor at atmospheric pressure and the composition of the effluent stream of the reactor was analyzed online by a mass spectrometer (MKS Cirrus) using an electron multiplier detector. A temperature program from room temperature to 350 °C with a ramp rate of 10 °C/min and a 2 h hold at 350 °C was used. TOFs were calculated using the methanol conversion (from the m/z = 31) obtained under differential conditions (by altering the catalyst mass to limit the steady-state conversion to ~15% of less) normalized per surface metal atom using the size-calculated dispersion to correct for the surface to bulk ratio. Only carbon monoxide (from the m/z = 28) and hydrogen (from the m/z = 2) were observed as products. No conversion was obtained using silica (no metal) as a catalyst under same conditions. A variety of postreaction experiments were conducted and these experiments involved (1) cooling the catalyst under helium and then repeating the reaction step and (2) cooling the catalyst under helium and then performing a temperature-programmed oxidation (TPO) to measure carbon dioxide generation from coke deposits. For TPO experiments (performed on the same reactor apparatus described above), a flow of 5 SCCM of oxygen and 45 SCCM of helium was used. A temperature program from room temperature to 350 or 500 °C with a ramp rate of 10 °C/min and a 1 h hold at the maximum temperature was used. The amount of coke deposits was calculated from the carbon dioxide signal (m/z = 44).

■ ASSOCIATED CONTENT

Supporting Information

Description of XAS data collection and analysis, XRD profiles as a function of Pd particle size, XANES and EXAFS region spectra as a function of Pd particle size, comparison of methanol conversion and coke formation reaction rates, and comparison of bulk and surface coordination numbers. This material is available free of charge via the Internet at http://pubs.acs.org.

■ AUTHOR INFORMATION

Corresponding Author

*Phone: (+1) 813-974-6498. E-mail: jnkuhn@usf.edu.

Notes

The authors declare no competing financial interest.

■ ACKNOWLEDGMENTS

Funding for this work, provided by NREL subcontract No.8 XGB-0-40646-01, Hinkley Center for Solid and Hazardous Waste Management, a Florida Energy Systems Consortium Seed Grant, and the USF Internal Awards Program under Grant No. 0074332, are gratefully acknowledged. Portions of this work were performed at the DuPont-Northwestern-Dow Collaborative Access Team (DND-CAT) located at Sector 5 of the Advanced Photon Source (APS). DND-CAT is supported by E.I. DuPont de Nemours & Co., The Dow Chemical Company and the State of Illinois. Use of the APS was supported by the U.S. Department of Energy, Office of Science, Office of Basic Energy Sciences, under contract number DE-AC02-06CH11357. Assistance from the DND-CAT beamline scientists, especially to Qing Ma, is greatly appreciated.

■ REFERENCES

(1) Boudart, M. *J. Mol. Catal.* **1985**, *30*, 27−38.
(2) Van Santen, R. A. *Acc. Chem. Res.* **2009**, *42*, 57−66.
(3) Somorjai, G. A.; Li, Y. *Introduction to Surface Chemistry and Catalysis*, 2nd ed.; John Wiley & Sons, Inc.: New York, 2010.
(4) Christopher, P.; Linic, S. *J. Am. Chem. Soc.* **2008**, *130*, 11264−11265.
(5) Tsung, C.-K.; Kuhn, J. N.; Huang, W.; Aliaga, C.; Hung, L.-I.; Somorjai, G. A.; Yang, P. *J. Am. Chem. Soc.* **2009**, *131*, 5817−5822.
(6) Tian, N. Z.; Sun, Z.-Y.; Ding, S.-G.; Wang, Y. *Science* **2007**, *316*, 732−735.
(7) Stamenkovic, V. R.; Fowler, B.; Mun, B. S.; Wang, G.; Ross, R. N.; Lucas, C. A.; Markovic, N. M. *Science* **2007**, *315*, 493−497.
(8) Fu, Q.; Saltsburg, H.; Flytzani-Stephanopoulos, M. *Science* **2003**, *301*, 935−938.
(9) Studt, F.; Abild-Pedersen, F.; Bligaard, T.; Sørensen, R. Z.; Christensen, C. H.; Nørskov, J. K. *Science* **2009**, *320*, 1320−1322.
(10) Alayoglu, S.; Eichhorn, B. W. *Nat. Mater.* **2008**, *7*, 333−338.
(11) Kuhn, J. N.; Huang, W.; Tsung, C.-K.; Zhang, Y.; Somorjai, G. A. *J. Am. Chem. Soc.* **2008**, *130*, 14026−14027.
(12) Yamada, Y.; Tsung, C.-K.; Huang, W.; Huo, Z.; Habas, S. E.; Soejima, T.; Aliaga, C. E.; Somorjai, G. A.; Yang, P. *Nature Chem.* **2011**, *3*, 372−376.
(13) Yin, Y. D.; Rioux, R. M.; Erdonmez, C. K.; Hughes, S.; Somorjai, G. A.; Alivisatos, A. P. *Science* **2004**, *304* (5671), 711−714.
(14) Joo, S. H.; Park, J. Y.; Tsung, C.-K.; Yamada, Y.; Yang, P.; Somorjai, G. A. *Nat. Mater.* **2008**, *8*, 126−131.
(15) Arnal, P. M.; Comotti, M.; Scuth, F. *Angew. Chem., Int. Ed.* **2006**, *45*, 8224−8227.
(16) Tang, L.; Han, B.; Persson, K.; Friesen, C.; He, T.; Sieradzki, K.; Ceder, G. *J. Am. Chem. Soc.* **2010**, *132*, 596−600.
(17) Zhang, J.; Sasaki, K.; Sutter, E.; Adzic, R. R. *Science* **2007**, *315*, 220−222.
(18) Report from the U.S. Department of Energy Office of Basic Energy Sciences Workshop. Basic Research Needs: Catalysis for Energy, August 6−8, 2007, Bethesda, MD, 1−59.
(19) Steele, B. C. H.; Heinzel, A. *Nature* **2001**, *414*, 345−352.
(20) Huber, G. W.; Iborra, S.; Corma, A. *Chem. Rev.* **2006**, *106*, 4044−4098.
(21) Che, M.; Bennett, C. O. *Adv. Catal.* **1989**, *36*, 55−172.
(22) Borg, O.; Dietzel, P. D. C.; Spjelkavik, A. I.; Tveten, E. Z.; Walmsley, J. C.; Diplas, S.; Eri, S.; Holmen, A.; Rytter, E. *J. Catal.* **2008**, *259*, 161−164.
(23) Bezemer, G. L.; Bitter, J. H.; Kuipers, H. P. C. E.; Oosterbeek, H.; Holewijn, J. E.; Xu, X.; Kapteijn, F.; van Dillen, A. J.; De Jong, K. P. *J. Am. Chem. Soc.* **2006**, *128*, 3956−3964.
(24) Zhang, Y.; Grass, M. E.; Habas, S. E.; Tao, F.; Zhang, T.; Yang, P.; Somorjai, G. A. *J. Phys. Chem. C* **2007**, *111*, 12243−12253.
(25) Teranishi, T.; Hosoe, M.; Tanaka, T.; Miyake, M. *J. Phys. Chem. B* **1999**, *103*, 3818−3827.

(26) Wang, Y.; Ren, J.; Deng, K.; Gui, L.; Tang, Y. *Chem. Mater.* **2000**, *12*, 1622−1627.
(27) Lim, B.; Jiang, M.; Camargo, P. H. C.; Cho, E. C.; Tao, J.; Lu, X.; Zhu, Y.; Xia, Y. *Science* **2009**, *324*, 1302−1305.
(28) Burda, C.; Chen, X.; Narayanan, R.; El-Sayed, M. A. *Chem. Rev.* **2005**, *105*, 1025−1102.
(29) Tew, M. W.; Miller, J. T.; Van Bokhoven, J. A. *J. Phys. Chem.C* **2009**, *113*, 15140−15147.
(30) Bartholomew, C. H.; Farrauto, R. J. *Fundamentals of Industrial Catalytic Processes*, 2nd ed.; John Wiley & Sons: Hoboken, NJ, 2006.
(31) Tao, A. R.; Habas, S. E.; Yang, P. *Small* **2008**, *4*, 310−325.
(32) Xia, Y.; Xiong, Y.; Lim, B.; Skrabalak, S. E. *Angew. Chem., Int. Ed.* **2009**, *48*, 60−103.
(33) Chen, J. G. *Surf. Sci. Rep.* **1997**, *30*, 1.
(34) Bligaard, T.; Norskov, J. K.; Dahl, S.; Matthiesen, J.; Christensen, C. H.; Sehested, J. *J. Catal.* **2004**, *224*, 206−217.
(35) Strong, K. L.; Anderson, D. P.; Lafdi, K.; Kuhn, J. N. *Carbon* **2003**, *41*, 1477.
(36) Chen, J. G.; Menning, C. A.; Zellner, M. B. *Surf. Sci. Rep.* **2008**, *63*, 201−254.
(37) Rostrup-Nielsen, J. R. *J. Catal.* **1984**, *85*, 31.
(38) Trimm, D. L. *Catal. Today* **1997**, *37*, 233.
(39) Bond, G. C. *Acc. Chem. Res.* **1993**, *26*, 490−195.
(40) Kitchin, J. R.; Norskov, J. K.; Barteau, M. A.; Chen, J. G. *Phys. Rev.* **2004**, *93*, 156801−156804.
(41) Mavrikakis, M.; Hammer, B.; Norskov, J. K. *Phys. Rev. Lett.* **1998**, *81*, 2819−2822.
(42) Harrison, W. A. *Electronic Structure and the Properties of Solids*, 2nd ed.; Dover Publications, Inc.: New York, 1989.
(43) Hammer, B.; Norskov, J. K. *Adv. Catal.* **2000**, *45*, 71−129.
(44) Van Santen, R. A.; Neurock, M.; Shetty, S. G. *Chem. Rev.* **2010**, *110*, 2007−2048.
(45) Ravel, B.; Newville, M. *J. Synchrotron Radiat.* **2005**, *12*, 537−541.
(46) Newville, M. *J. Synchrotron Radiat.* **2001**, *8*, 322−324.